Reversible Semimetal-semiconductor Transition of Unconventional-phase WS_2 Nanosheets

Wei Zhai[1†], Junlei Qi[2†], Chao Xu[3†], Bo Chen[1], Zijian Li[1], Yongji Wang[1], Li Zhai[1,4], Yao Yao[1], Siyuan Li[1], Qinghua Zhang[5], Yiyao Ge[1], Banlan Chi[1], Yi Ren[1], Zhiqi Huang[1], Zhuangchai Lai[1], Lin Gu[6], Ye Zhu[3]*, Qiyuan He[2]*, Hua Zhang[1,4,7]*

[1]Department of Chemistry, City University of Hong Kong, Hong Kong, China

[2]Department of Materials Science and Engineering, City University of Hong Kong, Hong Kong, China

[3]Department of Applied Physics and Research Institute for Smart Energy, The Hong Kong Polytechnic University, Hong Kong, China

[4]Hong Kong Branch of National Precious Metals Material Engineering Research Center (NPMM), City University of Hong Kong, Hong Kong, China

[5]Beijing National Laboratory for Condensed Matter Physics, Institute of Physics, Chinese Academy of Sciences, Beijing 100190, China

[6]Beijing National Center for Electron Microscopy and Laboratory of Advanced Materials, Department of Materials Science and Engineering, Tsinghua University, Beijing 100084, China

[7]Shenzhen Research Institute, City University of Hong Kong, Shenzhen, 518057, China

[†]These authors contributed equally to this work.

*Corresponding authors. E-mail: hua.zhang@cityu.edu.hk; qiyuanhe@cityu.edu.hk; ye.ap.zhu@polyu.edu.hk

Abstract:

Phase transition with bandgap modulation of materials has gained intensive research attention due to its various applications, including memories, neuromorphic computing, and transistors. As a powerful strategy to tune the crystal phase of transition metal dichalcogenides (TMDs), the phase transition of TMDs provides opportunities to prepare new phases of TMDs for exploring their phase-dependent property, function, and application. However, the previously reported phase transition of TMDs is mainly irreversible. Here, we report a reversible phase transition in the semimetallic 1T′-WS_2 driven by proton intercalation and deintercalation, resulting in a newly discovered semiconducting WS_2 with a novel unconventional phase, denoted as $1T'_d$ phase. Impressively, an on/off ratio of up to 10^6 has been achieved during the phase transition of WS_2 from the semimetallic 1T′ phase to the semiconducting $1T'_d$ phase. Our work not only provides a unique insight into the phase transition of TMDs *via* the proton intercalation, but also opens up possibilities to tune their physicochemical properties for various applications.

Text

Crystal phase is one essential structural parameter beyond size, dimensionality, morphology, and facet, that determines the physicochemical properties of nanomaterials.[1-2] As one of the powerful strategies in phase engineering of nanomaterials (PEN),[1] phase transition accompanied by bandgap modulation has been widely explored in various materials owing to its great potential for diverse fundamental studies and applications.[3-6] In particular, phase transition of transition metal dichalcogenides (TMDs) is intriguing owing to their unique crystal-phase-dependent electronic structures, leading to fundamental studies in catalysis,[7-8] (opto)electronics,[4,9] and condensed matter physics.[10-12] The phase transition of TMDs can be initialized by various methods,[1] such as chemical modification,[13] laser irradiation,[14] and lithium-ion intercalation.[15-16] However, due to the large energy difference between the thermodynamically stable phase (*e.g.*, 2H) and unconventional phase (*e.g.*, 1T and 1T′) in TMDs,[17] the phase transition in TMDs can only be realized in either monolayers or localized domains.[5,15,18] Moreover, the associated undesirable structural damages, such as amorphization,[19] vacancy generation,[14] and compositional alteration,[20] could lead to a poor reversibility of the phase transition. Until now, the reversible phase transition of TMDs has only been demonstrated in the transition-metal telluride under electrostatic gating by taking advantage of the small internal energy difference between their 2H and 1T′ phases.[4-5, 17, 21] However, a recent study has indicated that such strong gate modulation can induce the formation of Te vacancies.[20] Alternatively, intercalation strategies take advantage of the layered structure of TMDs by intercalating various guest species into the van der Waals gaps to achieve a phase transition in bulk crystals.[6,15,22,23] However, the reported intercalation methods, either chemical or electrochemical,[15, 24-27] can only induce phase transition in localized domains together with undesirable structural damages and limited reversibility. Despite these research efforts, the phase transition in TMDs across the single-crystal level with high controllability and reversibility remains a great challenge. Compared to the commonly used guest species, such as metal ion,[25] metal atom,[28] and molecule,[29] the smallest and lightest ion, proton, has attracted intensive research attention owing to its superior ability in tuning the physicochemical properties of nanomaterials for various applications.[3,30-32] For example, the hydrogenation of metal oxides *via* proton intercalation has been achieved, leading to the modulation of their properties.[3,30,33,34]

In this work, we report a highly efficient reversible phase transition strategy *via* the proton

intercalation and deintercalation in a microcell device (Figure 1a), in which the high electron injection and extraction densities (~ 1 e per formula unit of WS_2) can induce a reversible phase transition of the semimetallic 1T′-WS_2 (Figure 1b) across a single-crystalline nanosheet. By employing various *in-situ* and *ex-situ* characterizations, the resulting structure after the phase transition of 1T′-WS_2 has been identified as a new distorted octahedral phase, denoted as 1T′$_d$. Impressively, the obtained 1T′$_d$-WS_2 can be completely transferred to 1T′-WS_2 after the proton deintercalation, indicating that the reversible phase transition has been achieved in the single-crystalline 1T′-WS_2 nanosheet *via* proton intercalation and deintercalation. Moreover, a transport modulation with an on/off ratio of as high as 10^6 has been realized during the phase transition from the 1T′-WS_2 to 1T′$_d$-WS_2.

The reversible phase transition driven by the proton intercalation and deintercalation in 1T′-WS_2 nanosheets was conducted in microcell devices (Figures. 2a, S1 and S2). Figure S3 displays the detailed equivalent circuit diagram of the three-electrode microcell device shown in Figures 2a and S1a, in which the mechanically exfoliated 1T′-WS_2 nanosheet, Pt wire, and evaporated Cr/Au electrodes are used as the channel material, gate, and drain and source electrodes, respectively. Figure. 2b shows the typical drain-source current (I_{ds}, red curve) and the gate current (I_g, olive dotted curve) obtained in a 0.5 M H_2SO_4 aqueous solution used as the electrolyte. Initially, the 1T′-WS_2 maintains a stable and high conductance as the gate potential (V_g) ranging from 0 to 0.96 V, which is consistent with the semimetallic feature of 1T′-WS_2 under gating.[35] When the V_g exceeds 0.96 V, the I_{ds} reduces dramatically together with the appearance of positive spikes in I_g (purple area in Figure 2b), which corresponds to the electron injection into the 1T′-WS_2 nanosheet. When the V_g is scanned back from 1.4 V toward 0 V, the I_{ds} increases and finally reaches the initial current value along with negative spikes in I_g (light blue area in Figure 2b), which corresponds to the electron extraction from the WS_2 nanosheet. By integrating the gate current profile in Figure 2b to calculate the numbers of injected and extracted electrons, it is found that the number of injected electrons is nearly equal to that of the extracted ones (Figure S4). It is also worth mentioning that both the electron injection and extraction densities in 1T′-WS_2 are ~ 1 e per formula unit of WS_2, which are ~ 5 times that obtained in the most efficient reversible electron injection and extraction strategy reported previously, *i.e.*, the electrostatic electron injection and extraction in $MoTe_2$.[36]

To further clarify the origin of such a significant electrical transport modulation and the charge transfer process at the solid-electrolyte interface (SEI), we fabricated microcell devices with different windows, in which different parts of nanosheets were exposed to the electrolyte (Figure 2c). It is worth mentioning that the electrical transport modulation and the electron transfer cannot occur on the device without a window (Figures 2c-I and 2d-I), suggesting the effective passivation of the poly(methyl methacrylate) (PMMA) layer. When a window, which is exposed to the electrolyte, is open only on the basal plane of the 1T′-WS_2 nanosheet (Figure 2c-II), no electrical transport modulation and electron transfer are observed (Figures 2c-II and 2d-II), indicating that the electrostatic gating has no effect on the transport modulation of the 1T′-WS_2 nanosheet.[37] However, the transport modulation and electron transfer can occur in a device with one (Figures 2c-III and 2d-III) or two edges (Figures 2c-IV and 2d-IV) of the 1T′-WS_2 nanosheet in the opened window, indicating that the transport modulation and electron transfer originate from the proton intercalation and deintercalation through the edge of 1T′-WS_2 nanosheet. In addition, when the V_g exceeds 0.96 V, the decay slope of I_{ds} in Figure 2c-III can reach as low as 16 mV/dec, which is much lower than the room-temperature Boltzmann limit of 60 mV/dec in electrostatic gating,[38] further confirming that the electrical transport modulation is not from the electrostatic gating. Based on our aforementioned experiments and the previous on-chip studies on the TMD intercalation,[27] it is believed that the charge injection and extraction in the H_2SO_4 aqueous solution can be attributed to the intercalation and deintercalation of protons, respectively, which is the only cation in the electrolyte solution, in the van der Waals gaps of the layered 1T′-WS_2 nanosheets. Our result is similar to the phase transition in metal oxides induced by hydrogenation in which protons are intercalated in their atomic lattices.[3,30-34] Our further experiments on other ion-containing electrolytes demonstrate that only the electrolyte containing protons leads to this reversible electrical transport modulation (Figure S5). Additionally, unlike other ionic or molecular intercalations, which normally damage the structural integrity of 2D crystals,[14-16,20] the proton intercalation and deintercalation are highly reversible, as evidenced by the cycling test (Figures S6 and S7). Previous studies have highlighted the structural diversity of TMD crystals and the importance of the electron injection in the modulation of their crystal structures.[1-2] To further understand how high electron injection and extraction densities can lead to such large transport modulation, *in-situ* Raman characterization was employed to characterize the structural evolution of 1T′-WS_2 during the proton

intercalation and deintercalation (Figure S1e,f). Figure 3a shows the Raman spectra of the 1T′-WS_2 nanosheet before intercalation (blue curve, V_g = 0 V), the intercalated nanosheet (red curve, V_g = 1.5 V), and the de-intercalated nanosheet (green curve, V_g = 0 V) in 0.5 M H_2SO_4 aqueous electrolyte. The 1T′-WS_2 nanosheet before intercalation shows a characteristic Raman spectrum of 1T′-WS_2 (blue curve), indicating the high phase purity of the exfoliated nanosheets.[35] When the nanosheet is intercalated (V_g = 1.5 V), the peaks indexed to 1T′-WS_2 disappear entirely (red curve). Instead, a new set of distinct Raman peaks located at 128, 212, 263, 282, 298, 317 and 407 cm^{-1} emerged, indicating a crystal structure change of the WS_2 nanosheet. When the V_g is swept back to 0 V, the nanosheet is de-intercalated, and the corresponding Raman spectrum (green curve) is identical to that of the 1T′-WS_2 nanosheet before intercalation (blue curve), suggesting the high reversibility of such a structural transition. It is worth mentioning that the set of Raman peaks emerged at V_g = 1.5 V is different from that in previously reported WS_2 polymorphs, indicating the formation of a new phase of WS_2.

As shown in the *in-situ* photoluminescence (PL) measurement (blue curve in Figure 3b), there is no PL signal on the 1T′-WS_2 nanosheet before intercalation, which originates from its semimetallic nature.[35] In contrast, the intercalated WS_2 nanosheet exhibits a semiconducting characteristic with a strong PL peak of ~ 650 nm at V_g = 1.5 V (red curve in Figure 3b). After V_g is swept back to 0 V, the absence of the PL signal (green curve in Figure 3b) manifests the de-intercalated nanosheet has transformed from the semiconducting phase to the semimetallic 1T′ phase, indicating the high reversibility of the phase transition.

The phase transition processes can also be visualized in a voltage mapping in which the Raman spectra of the WS_2 nanosheet were recorded during the V_g swept from 0 to 1.5 V with an interval of 0.1 V. To make the phase transition visible, Raman intensities obtained at different voltages have been normalized. As shown in Figure 3c, the WS_2 nanosheet remains in the pristine 1T′ phase and shows its characteristic peaks at 112, 179, 239, 268, 316, and 407 cm^{-1} when a constant V_g ranging from 0 to 0.8 V was applied. At V_g = 0.9 V, the Raman peaks corresponding to 1T′-WS_2 disappear while those located at 129, 212, 263, 282, 298, 317 and 407 cm^{-1} emerged which can be assigned to the new phase. Such a phase transition process is consistent with the sharp drop of I_{ds} in the electrical transport measurement (Figure 2b). According to the aforementioned PL and Raman spectra, the observed large electrical

transport modulation shown in Figure 2b can be attributed to the modulation of electronic band structures from semimetal to semiconductor. The aforementioned phase transition is different from that induced by electrostatic gating, in which the phase percentages gradually change and also strongly correlate with the gate potential.[5]

As shown in Figure 3c, the nanosheet maintains the same new phase when the V_g ranges from 0.9 to 1.5 V. As the V_g is swept back to 0.8 V, the Raman peaks indexed to the new phase disappear and the peaks belonging to 1T′-WS_2 reappear, indicating the phase of WS_2 nanosheet is transformed back to the original 1T' phase. The phase percentages at different voltages determined according to $\frac{S_{1T'}}{S_{1T'}+S_{1T'_d}}$, where $S_{1T'}$ and $S_{1T'_d}$ represent the areas of Raman peaks assigned to the 1T′ phase at 112 cm^{-1} and the new 1T′$_d$ phase at 128 cm^{-1}, further consolidate this result. As shown in Figure 3d, at the V_g ranging from 0 to 0.8 V, the percentage of 1T′ phase is 100%. However, it approaches to ~ 0% at the V_g ranging from 0.9 to 1.5 V. To further identify the phase transition process at the V_g ranging from 0.8 and 0.9 V, detailed Raman characterization was carried out at V_g = 0.81 V and 0.82 V (Figure S8). The Raman spectrum recorded at V_g = 0.81 V demonstrates the coexistence of the 1T′ phase and the new phase (Figure S8a), while the phase of the WS_2 nanosheet completely transforms to the new phase when the V_g slightly increases to 0.82 V from 0.81 V (Figure S8b).

The highly reverible phase transition in the aqueous proton electrolyte hinders the *ex-situ* structural anylysis of the phase after proton intercalation. To stabilize the intercalated structure, the proton intercalation was performed in an organic proton electrolyte with more slugglish intercalation and deintercalation speeds.[39-40] Similar to the result obtained in the H_2SO_4 aqueous electrolyte, the I_{ds} remains constant and starts to drop upon V_g reaching a threshold voltage (V_g = 1.1 V, Figure S9a). The nanosheet transforms from a high conductance state to a low conductance state. After the intercaltion process (V_g was swept from 0 to 3 V), the gate electrode was immediately removed out of the electrolyte and the I_{ds}-V_{ds} (red curve in Figure S9b) of the WS_2 nanosheet was measured. As shown in Figure S9b, at V_{ds} = 0.10 V, the I_{ds} drops from 0.24 mA before the proton intercalation to 7.52×10^{-8} mA after the proton intercalation, showing an on/off ratio of over 10^6. The large intercalation voltage range (0.96 to 2.01 V, Figure S9a), compared to that (0.96 to 1.15 V) obtained in the 0.5 M H_2SO_4 aqueous electrolyte (Figure 2b), which is consistent with the sluggish intercalation kinetics in the

organic electrolyte.[40] It is also worth mentioning that the WS_2 nanosheet intercalated in the organic proton electrolyte shows a similar Raman spectrum compared to that intercalated in the H_2SO_4 aqueous electrolyte (Figure S10), indicating that WS_2 nanosheets intercalated in the H_2SO_4 aqueous solution and the organic proton electrolyte should have a similar structure. Importantly, the well-maintained low conductance of the nanosheets after the proton intercalation in the organic electrolyte (red curve in Figure S9b) indicates that the obtained intercalated compound in the organic proton electrolyte can be maintained, making it possible to characterize the detailed atomic structures by transmission electron microscope (TEM).

To disclose the atomic structure of the new phase, atomic-resolution high-angle annular dark-field scanning TEM (HAADF-STEM) and selected area electron diffraction (SAED) were used to characterize the structure change of WS_2 nanosheet before and after its intercalation in the organic proton electrolyte. As shown in Figure 4a, the nanosheet before intercalation exhibits a typical diffraction pattern of the 1T′ phase, showing a lower symmetrical $1\times\sqrt{3}$ rectangular supercell compared to the 1T phase. As shown in the HAADF-TEM image (Figure 4b), the structure of 1T′-WS_2 before intercalation is directly reflected by the zigzag chains consisting of two lines of W columns. The intra-line W-W column distance within the chain is 0.32 nm (Figure S11a), which is consistent with the crystal structure refined from single crystal X-ray diffraction in our previous report.[35] The corresponding fast Fourier transform (FFT) pattern (Figure 4c) of the HAADF-STEM image in Figure 4b also shows the same supercell with the SAED pattern. After the proton intercalation, a new group of superspots appears in the SAED pattern (highlighted by red circles in Figure 4d), indicating the phase transition from 1T′ to a new structure with a decreased symmetry. The well-preserved zigzag chains in the HAADF-STEM image (Figure 4e) indicate that no structure damage was introduced and only a distortion occurs in the 1T′-WS_2 nanosheet after the proton intercalation, resulting in a decreased symmetry. The corresponding FFT pattern in Figure 4f displays consistent diffraction peaks with the SAED pattern in Figure 4d. To disentangle the structural distortion, phase lock-in analysis[41] was performed on the high-resolution STEM image (Figure 4e). A reference image resembling the 1T′ lattice (Figure S12) is generated by damping the amplitude of the new superspots in the FFT pattern (indicated by red circles in Figure 4f) to the background level. Afterward, an inverse Fourier transform is applied. The distortion of reference lattice is then excluded. The relative atomic displacement with

respect to the reference lattice can be derived by fitting the column positions using 2D Gaussian function, which can quantitatively describe the lattice distortion caused by proton intercalation. The displacement vector field is visualized by arrows in Figure 4g. According to the displacement map, four occupation columns of W stained with four different colors can be classified (Figure 4h), and their displacements are counted in Figure 4i. The columns stained with magenta and green move the most significantly in opposite directions along [010] and [$0\bar{1}0$] by an average distance of 0.13 and 0.11 Å, respectively, while those stained with cyan and red move just slightly and roughly along a perpendicular direction by an average distance of 0.03 and 0.03 Å. The displacement leads to the formation of one line of W dimers (Figures 4g and S11b) within the W-W zigzag chains, which ambiguously demonstrates a new distorted octahedral structure, denoted as 1T′$_d$, that is distinct from all the reported phases in WS_2. Impressively, the phase transition can occur across the whole nanosheet, demonstrating that the nanosheet has completely transformed from the 1T′ phase to the new 1T′$_d$ phase (Figure S13).

Conclusion

We have demonstrated a reversible phase transition strategy driven by proton intercalation and deintercalation, respectively, to inject into and extract electrons out of 1T′-WS_2. The high electron injection and extraction densities (~ 1 e per formula unit of WS_2) driven by the proton intercalation and deintercalation enable a completely reversible phase transition between 1T′-WS_2 and the new 1T′$_d$-WS_2, which is confirmed by comprehensive characterizations, including Raman, PL, SAED, and HAADF-STEM. Such a reversible phase transition driven by the proton intercalation and deintercalation opens a new strategy toward the dynamical control of the phase-dependent physicochemical properties of TMDs, which might exhibit further applications in transistors, memory devices, and neuromorphic computing.

Acknowledgments

H.Z. thanks the support from the Project 52131301 supported by NSFC, the Science Technology and Innovation Committee of Shenzhen Municipality (grant no. JCYJ20200109143412311, and grant no. SGDX2020110309300301, “Preparation of single atoms on transition metal chalcogenides for electrolytic hydrogen evolution”, CityU), ITC via the Hong Kong Branch of National Precious Metals

Material Engineering Research Center (NPMM), the Research Grants Council of Hong Kong (AoE/P-701/20, GRF Project No. 11315722), the Start-Up Grant (Project No. 9380100) and the grants (Project Nos. 9680314, 9678272, 7020013, 7020054 and 1886921) from the City University of Hong Kong. Q.H. acknowledges the funding support from Research Grants Council of Hong Kong (Early Career Scheme Project No. 21302821 and GRF Project No. 11314322), and the StartUp Grant (Project No. 9610482) and the grants (7005468 and 9229079) from the City University of Hong Kong. Y.Z. Thanks for the grant (No. ZVRP) from Hong Kong Polytechnic University. The authors also thank Professor J. S. Zhang (Tsinghua University) for discussing how to design a passivation layer to suppress the noise current.

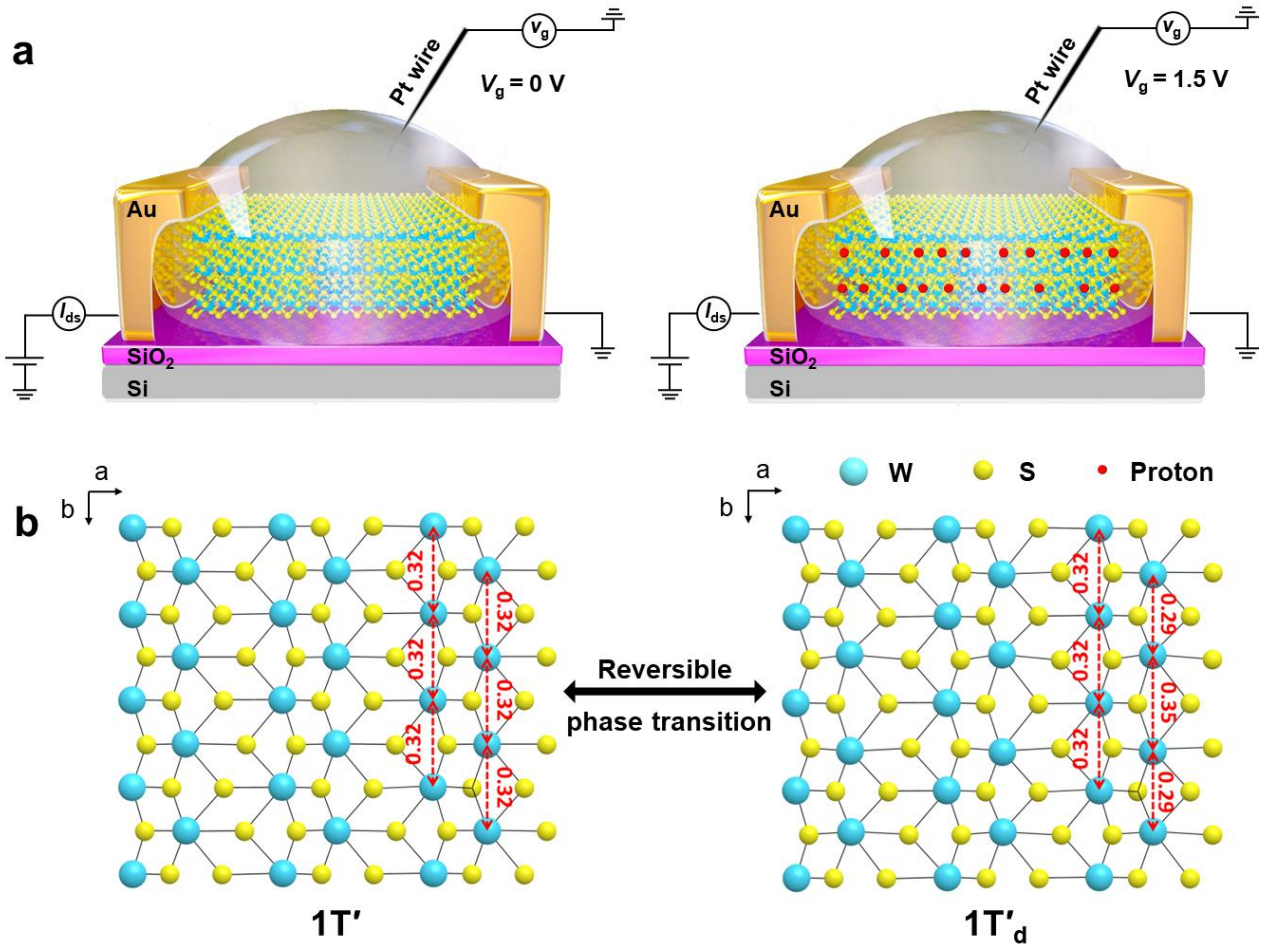

Figure 1. Schematic illustration of reversible phase transition of 1T′-WS_2 conducted in a microcell device. (a) Schematic illustration of the microcell device used for the reversible phase transition of 1T′-WS_2 driven by the proton intercalation and deintercalation, respectively. (b) The atomic structural models of 1T′-WS_2 and 1T′$_d$-WS_2 during the reversible phase transition.

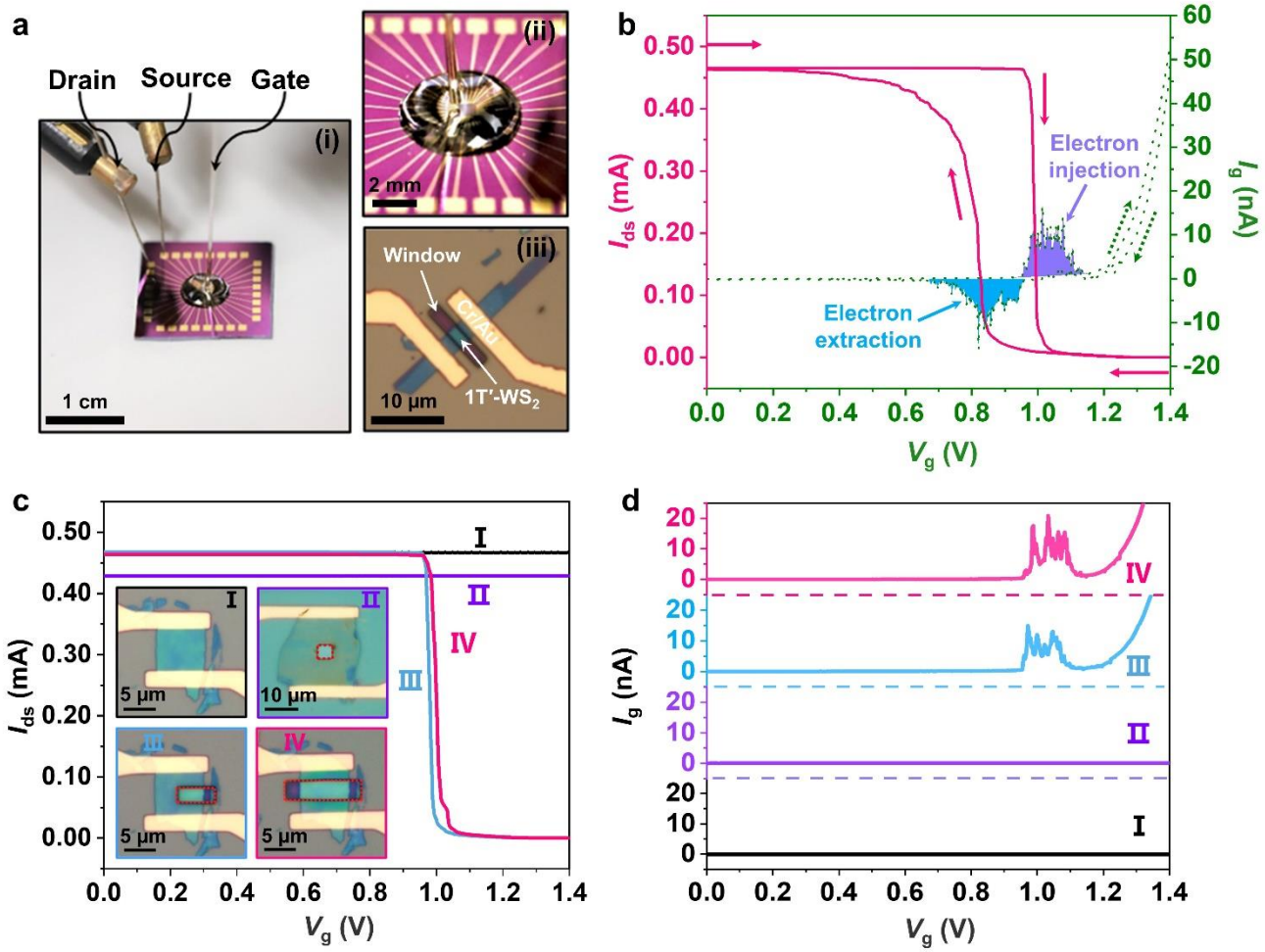

Figure 2. Microcell devices measured during the electron injection and extraction . (a) Optical images of a microcell device: the overall set-up with three electrodes (i), the high-magnification image of the microcell device with a droplet of electrolyte (ii), and the device fabricated with a mechanically exfoliated 1T′-WS_2 nanosheet with a window opened in the PMMA passivation layer, in which two opposite edges and the basal plane of 1T′-WS_2 nanosheet are exposed to the electrolyte (iii). (b) Typical drain-source current (I_{ds}, red curve) and gate current (I_g, olive dotted curve) measured in the fabricated microcell device of 1T′-WS_2 during the charge injection and extraction processes in a 0.5 M H_2SO_4 aqueous solution. (c) Typical drain-source current (I_{ds}) curves of 1T′-WS_2 nanosheets in different windows swept in a 0.5 M H_2SO_4 aqueous solution. Insets: optical images of electric devices without window (I) and with different windows (II-IV). The red dotted areas represent the windows opened in the PMMA passivation layers. (d) Typical I_g *vs.* V_g curves of 1T′-WS_2 nanosheets swept in a 0.5 M H_2SO_4 aqueous solution in different windows shown in the inset in (c).

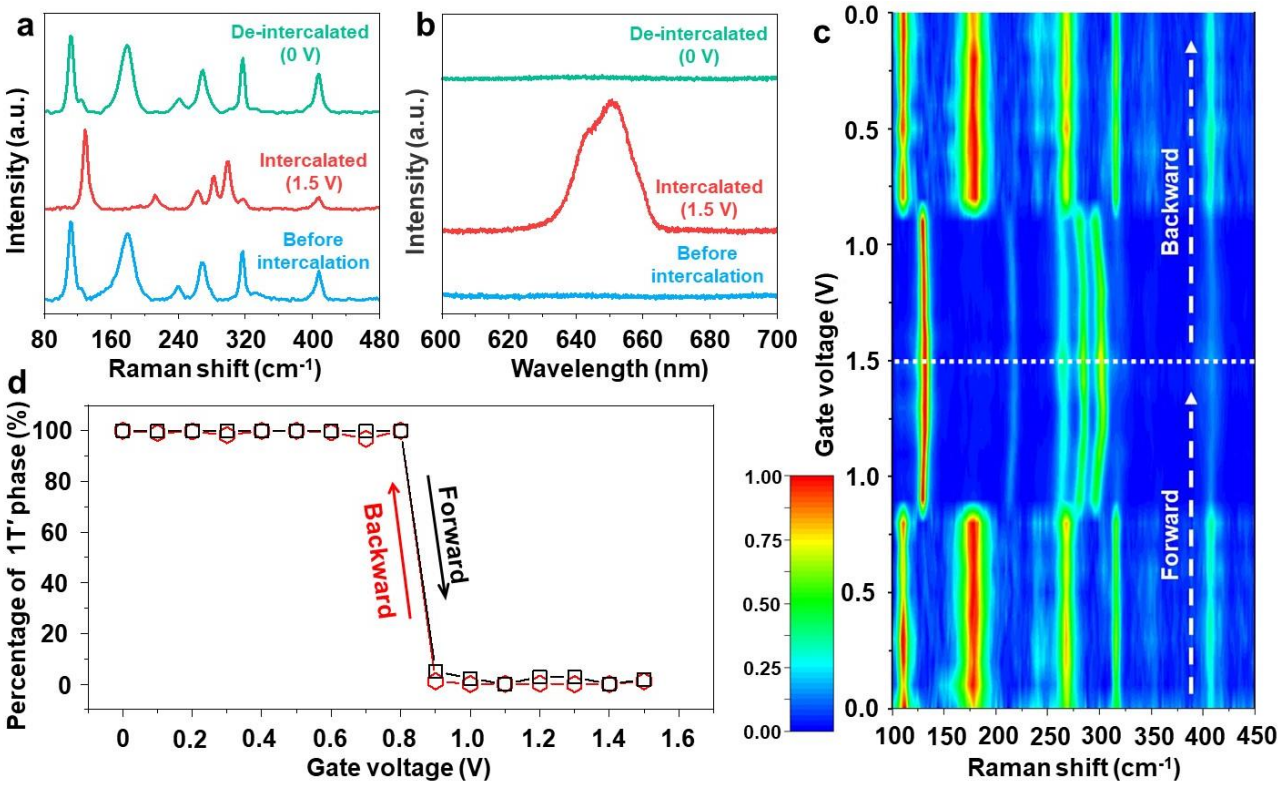

Figure 3. Characterization of the phase transition of 1T′-WS_2 nanosheets. (a) *In-situ* Raman characterization of the 1T′-WS_2 nanosheet during the proton intercalation and deintercalation in a 0.5 M H_2SO_4 aqueous solution. (b) *In-situ* photoluminescence characterization of the 1T′-WS_2 nanosheet during the proton intercalation and deintercalation in a 0.5 M H_2SO_4 aqueous solution. (c) *In-situ* Raman spectra obtained at different gate potentials, showing a highly reversible phase transition process. (d) The percentage of 1T′ phase in the WS_2 nanosheet at different gate potentials. The percentage of the 1T′ phase is determined according to $\frac{S_{1T'}}{S_{1T'}+S_{1T'_d}}$, where $S_{1T'}$ and $S_{1T'_d}$ represent the areas of Raman peaks assigned to the 1T′ phase at 112 cm^{-1} and the new 1T′$_d$ phase at 128 cm^{-1}, respectively.

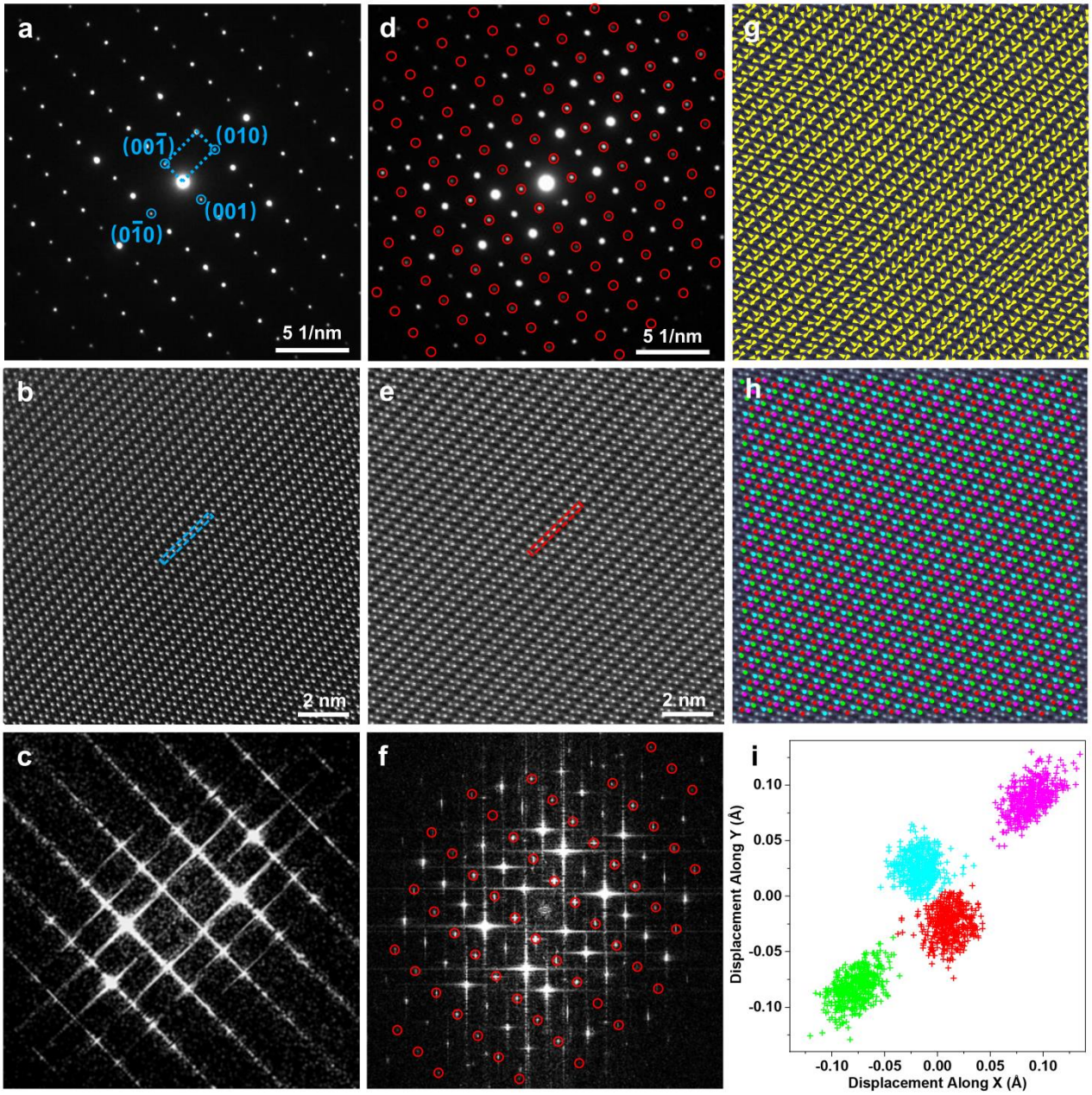

Figure 4. Structural characterization of 1T′-WS_2 and 1T′$_d$-WS_2 nanosheets. (a) SAED pattern, and (b) HAADF-STEM image of the 1T′-WS_2 nanosheet obtained *via* mechanical exfoliation of a bulk 1T′-WS_2 crystal. (c) The corresponding FFT pattern of the HAADF-STEM image in (b). (d) SAED pattern and (e) HAADF-STEM image of the 1T′-WS_2 nanosheet after proton intercalation. (f) The corresponding FFT pattern of the HAADF-STEM image in (e). (g) Relative displacement map of W columns in WS_2 nanosheet after proton intercalation with respect to the 1T′ lattice used as reference. (h) Occupation columns of W after proton intercalation. (i) Statistic distribution of the W column displacement.

Reference

(1) Chen, Y.; Lai, Z.; Zhang, X.; Fan, Z.; He, Q.; Tan, C.; Zhang, H., Phase engineering of nanomaterials. *Nat. Rev. Chem.* **2020**, *4*, 243-256.

(2) Voiry, D.; Mohite, A.; Chhowalla, M., Phase engineering of transition metal dichalcogenides. *Chem. Soc. Rev.* **2015**, *44*, 2702-12.

(3) Lu, N.; Zhang, P.; Zhang, Q.; Qiao, R.; He, Q.; Li, H.-B.; Wang, Y.; Guo, J.; Zhang, D.; Duan, Z.; Li, Z.; Wang, M.; Yang, S.; Yan, M.; Arenholz, E.; Zhou, S.; Yang, W.; Gu, L.; Nan, C.-W.; Wu, J.; Tokura, Y.; Yu, P., Electric-field control of tri-state phase transformation with a selective dual-ion switch. *Nature* **2017**, *546*, 124-128.

(4) Wang, Y.; Xiao, J.; Chung, T.-F.; Nie, Z.; Yang, S.; Zhang, X., Direct electrical modulation of second-order optical susceptibility via phase transitions. *Nat. Electron.* **2021**, *4* (10), 725-730.

(5) Wang, Y.; Xiao, J.; Zhu, H.; Li, Y.; Alsaid, Y.; Fong, K. Y.; Zhou, Y.; Wang, S.; Shi, W.; Wang, Y.; Zettl, A.; Reed, E. J.; Zhang, X., Structural phase transition in monolayer $MoTe_2$ driven by electrostatic doping. *Nature* **2017**, *550*, 487-491.

(6) Acerce, M.; Voiry, D.; Chhowalla, M., Metallic 1T phase MoS_2 nanosheets as supercapacitor electrode materials. *Nat. Nanotechnol.* **2015**, *10* (4), 313-318.

(7) Yu, Y.; Nam, G.-H.; He, Q.; Wu, X.-J.; Zhang, K.; Yang, Z.; Chen, J.; Ma, Q.; Zhao, M.; Liu, Z.; Ran, F.-R.; Wang, X.; Li, H.; Huang, X.; Li, B.; Xiong, Q.; Zhang, Q.; Liu, Z.; Gu, L.; Du, Y.; Huang, W.; Zhang, H., High phase-purity 1T′-MoS_2- and 1T′-$MoSe_2$-layered crystals. *Nat. Chem.* **2018**, *10*, 638-643.

(8) Voiry, D.; Yamaguchi, H.; Li, J.; Silva, R.; Alves, D. C.; Fujita, T.; Chen, M.; Asefa, T.; Shenoy, V. B.; Eda, G.; Chhowalla, M., Enhanced catalytic activity in strained chemically exfoliated WS_2 nanosheets for hydrogen evolution. *Nat. Mater.* **2013**, *12*, 850-5.

(9) Xu, X.; Pan, Y.; Liu, S.; Han, B.; Gu, P.; Li, S.; Xu, W.; Peng, Y.; Han, Z.; Chen, J.; Gao, P.; Ye, Y., Seeded 2D epitaxy of large-area single-crystal films of the van der Waals semiconductor 2H $MoTe_2$. *Science* **2021**, *372*, 195-200.

(10) Wang, W.; Kim, S.; Liu, M.; Cevallos, F. A.; Cava, R. J.; Ong, N. P., Evidence for an edge supercurrent in the Weyl superconductor $MoTe_2$. *Science* **2020**, *368*, 534-537.

(11) Yuan, Y.; Pan, J.; Wang, X.; Fang, Y.; Song, C.; Wang, L.; He, K.; Ma, X.; Zhang, H.; Huang, F.; Li, W.; Xue, Q.-K., Evidence of anisotropic Majorana bound states in 2M-WS_2. *Nat. Phy.* **2019**, *15*, 1046-1051.

(12) Vaňo, V.; Amini, M.; Ganguli, S. C.; Chen, G.; Lado, J. L.; Kezilebieke, S.; Liljeroth, P., Artificial heavy fermions in a van der Waals heterostructure. *Nature* **2021**, *599*, 582-586.

(13) Voiry, D.; Goswami, A.; Kappera, R.; Silva, C. d. C. C. e.; Kaplan, D.; Fujita, T.; Chen, M.; Asefa, T.; Chhowalla, M., Covalent functionalization of monolayered transition metal dichalcogenides by phase engineering. *Nat. Chem.* **2015**, *7*, 45-49.

(14) Cho, S.; Kim, S.; Kim, J. H.; Zhao, J.; Seok, J.; Keum, D. H.; Baik, J.; Choe, D.-H.; Chang, K. J.; Suenaga, K.; Kim, S. W.; Lee, Y. H.; Yang, H., Phase patterning for ohmic homojunction contact in $MoTe_2$. *Science* **2015**, *349*, 625-628.

(15) Eda, G.; Fujita, T.; Yamaguchi, H.; Voiry, D.; Chen, M.; Chhowalla, M., Coherent Atomic and Electronic Heterostructures of Single-Layer MoS_2. *ACS Nano* **2012**, *6*, 7311-7317.

(16) Xiong, F.; Wang, H.; Liu, X.; Sun, J.; Brongersma, M.; Pop, E.; Cui, Y., Li Intercalation in MoS_2: In Situ Observation of Its Dynamics and Tuning Optical and Electrical Properties. *Nano Lett.* **2015**, *15*, 6777-6784.

(17) Duerloo, K. A.; Li, Y.; Reed, E. J., Structural phase transitions in two-dimensional Mo- and W-dichalcogenide monolayers. *Nat. Commun.* **2014**, *5*, 4214.

(18) Lin, Y.-C.; Dumcenco, D. O.; Huang, Y.-S.; Suenaga, K., Atomic mechanism of the semiconducting-to-metallic phase transition in single-layered MoS_2. *Nat. Nanotechnol.* **2014**, *9*, 391-396.

(19) Zhang, X.; Luo, Z.; Yu, P.; Cai, Y.; Du, Y.; Wu, D.; Gao, S.; Tan, C.; Li, Z.; Ren, M.; Osipowicz, T.; Chen, S.; Jiang, Z.; Li, J.; Huang, Y.; Yang, J.; Chen, Y.; Ang, C. Y.; Zhao, Y.; Wang, P.; Song, L.; Wu, X.; Liu, Z.; Borgna, A.; Zhang, H.,

Lithiation-induced amorphization of $Pd_3P_2S_8$ for highly efficient hydrogen evolution. *Nat. Catal.* **2018**, *1*, 460-468.
(20) Zakhidov, D.; Rehn, D. A.; Reed, E. J.; Salleo, A., Reversible Electrochemical Phase Change in Monolayer to Bulk-like $MoTe_2$ by Ionic Liquid Gating. *ACS Nano* **2020**, *14*, 2894-2903.
(21) Zhang, F.; Zhang, H.; Krylyuk, S.; Milligan, C. A.; Zhu, Y.; Zemlyanov, D. Y.; Bendersky, L. A.; Burton, B. P.; Davydov, A. V.; Appenzeller, J., Electric-field induced structural transition in vertical $MoTe_2$- and $Mo_{1-x}W_xTe_2$-based resistive memories. *Nat. Mater.* **2019**, *18*, 55-61.
(22) Zhou, J.; Lin, Z.; Ren, H.; Duan, X.; Shakir, I.; Huang, Y.; Duan, X., Layered Intercalation Materials. *Adv. Mater.* **2021,** *33*, 2004557.
(23) Wu, Y.; Li, D.; Wu, C.-L.; Hwang, H. Y.; Cui, Y., Electrostatic gating and intercalation in 2D materials. *Nat. Rev. Mater.* **2023**, *8*, 41-53.
(24) Kappera, R.; Voiry, D.; Yalcin, S. E.; Branch, B.; Gupta, G.; Mohite, A. D.; Chhowalla, M., Phase-engineered low-resistance contacts for ultrathin MoS_2 transistors. *Nat. Mater.* **2014**, *13*, 1128-1134.
(25) Zeng, Z.; Yin, Z.; Huang, X.; Li, H.; He, Q.; Lu, G.; Boey, F.; Zhang, H., Single-layer semiconducting nanosheets: high-yield preparation and device fabrication. *Angew. Chem.* **2011**, *123*, 11289-11293.
(26) Wang, C.; He, Q.; Halim, U.; Liu, Y.; Zhu, E.; Lin, Z.; Xiao, H.; Duan, X.; Feng, Z.; Cheng, R.; Weiss, N. O.; Ye, G.; Huang, Y.-C.; Wu, H.; Cheng, H.-C.; Shakir, I.; Liao, L.; Chen, X.; Goddard Iii, W. A.; Huang, Y.; Duan, X., Monolayer atomic crystal molecular superlattices. *Nature* **2018**, *555*, 231-236.
(27) He, Q.; Lin, Z.; Ding, M.; Yin, A.; Halim, U.; Wang, C.; Liu, Y.; Cheng, H.-C.; Huang, Y.; Duan, X., In Situ Probing Molecular Intercalation in Two-Dimensional Layered Semiconductors. *Nano Lett.* **2019**, *19*, 6819-6826.
(28) Gong, Y.; Yuan, H.; Wu, C.-L.; Tang, P.; Yang, S.-Z.; Yang, A.; Li, G.; Liu, B.; van de Groep, J.; Brongersma, M. L.; Chisholm, M. F.; Zhang, S.-C.; Zhou, W.; Cui, Y., Spatially controlled doping of two-dimensional SnS_2 through intercalation for electronics. *Nat. Nanotechnol.* **2018**, *13*, 294-299.
(29) Qian, Q.; Ren, H.; Zhou, J.; Wan, Z.; Zhou, J.; Yan, X.; Cai, J.; Wang, P.; Li, B.; Sofer, Z.; Li, B.; Duan, X.; Pan, X.; Huang, Y.; Duan, X., Chiral molecular intercalation superlattices. *Nature* **2022**, *606*, 902-908.
(30) Li, L.; Wang, M.; Zhou, Y.; Zhang, Y.; Zhang, F.; Wu, Y.; Wang, Y.; Lyu, Y.; Lu, N.; Wang, G.; Peng, H.; Shen, S.; Du, Y.; Zhu, Z.; Nan, C.-W.; Yu, P., Manipulating the insulator–metal transition through tip-induced hydrogenation. *Nat. Mater.* **2022**, *21*, 1246-1251.
(31) Zhao, Q.; Liu, L.; Yin, J.; Zheng, J.; Zhang, D.; Chen, J.; Archer, L. A., Proton Intercalation/De-Intercalation Dynamics in Vanadium Oxides for Aqueous Aluminum Electrochemical Cells. *Angew. Chem. Int. Ed.* **2020,** *59*, 3048-3052.
(32) Wang, X.; Xie, Y.; Tang, K.; Wang, C.; Yan, C., Redox Chemistry of Molybdenum Trioxide for Ultrafast Hydrogen-Ion Storage. *Angew. Chem. Int. Ed.* **2018**, *57*, 11569-11573.
(33) Tan, A. J.; Huang, M.; Avci, C. O.; Büttner, F.; Mann, M.; Hu, W.; Mazzoli, C.; Wilkins, S.; Tuller, H. L.; Beach, G. S. D., Magneto-ionic control of magnetism using a solid-state proton pump. *Nat. Mater.* **2019**, *18*, 35-41.
(34) Huang, M.; Hasan, M. U.; Klyukin, K.; Zhang, D.; Lyu, D.; Gargiani, P.; Valvidares, M.; Sheffels, S.; Churikova, A.; Büttner, F.; Zehner, J.; Caretta, L.; Lee, K.-Y.; Chang, J.; Wang, J.-P.; Leistner, K.; Yildiz, B.; Beach, G. S. D., Voltage control of ferrimagnetic order and voltage-assisted writing of ferrimagnetic spin textures. *Nat. Nanotechnol.* **2021**, *16*, 981-988.
(35) Lai, Z.; He, Q.; Tran, T. H.; Repaka, D. V. M.; Zhou, D. D.; Sun, Y.; Xi, S.; Li, Y.; Chaturvedi, A.; Tan, C.; Chen, B.; Nam, G. H.; Li, B.; Ling, C.; Zhai, W.; Shi, Z.; Hu, D.; Sharma, V.; Hu, Z.; Chen, Y.; Zhang, Z.; Yu, Y.; Renshaw Wang, X.; Ramanujan, R. V.; Ma, Y.; Hippalgaonkar, K.; Zhang, H., Metastable 1T'-phase group VIB transition metal dichalcogenide crystals. *Nat. Mater.* **2021**, *20*, 1113-1120.
(36) Ye, J. T.; Zhang, Y. J.; Akashi, R.; Bahramy, M. S.; Arita, R.; Iwasa, Y., Superconducting Dome in a Gate-Tuned Band Insulator. *Science* **2012**, *338*, 1193-1196.
(37) Perera, M. M.; Lin, M.-W.; Chuang, H.-J.; Chamlagain, B. P.; Wang, C.; Tan, X.; Cheng, M. M.-C.; Tománek, D.;

Zhou, Z., Improved Carrier Mobility in Few-Layer MoS_2 Field-Effect Transistors with Ionic-Liquid Gating. *ACS Nano* **2013**, *7*, 4449-4458.
(38) Illarionov, Y. Y.; Knobloch, T.; Jech, M.; Lanza, M.; Akinwande, D.; Vexler, M. I.; Mueller, T.; Lemme, M. C.; Fiori, G.; Schwierz, F.; Grasser, T., Insulators for 2D nanoelectronics: the gap to bridge. *Nat. Commun.* **2020**, *11*, 3385.
(39) Li, S.; Li, J.; Wang, Y.; Yu, C.; Li, Y.; Duan, W.; Wang, Y.; Zhang, J., Large transport gap modulation in graphene via electric-field-controlled reversible hydrogenation. *Nat. Electron.* **2021**, *4*, 254-260.
(40) He, P.; Zhang, X.; Wang, Y.-G.; Cheng, L.; Xia, Y.-Y., Lithium-Ion Intercalation Behavior of $LiFePO_4$ in Aqueous and Nonaqueous Electrolyte Solutions. *J. Electrochem. Soc.* **2008**, *155*, A144.
(41) Goodge, B. H.; El Baggari, I.; Hong, S. S.; Wang, Z.; Schlom, D. G.; Hwang, H. Y.; Kourkoutis, L. F., Disentangling Coexisting Structural Order Through Phase Lock-In Analysis of Atomic-Resolution STEM Data. *Microsc. Microanal.* **2022**, *28*, 404-411.

TOC

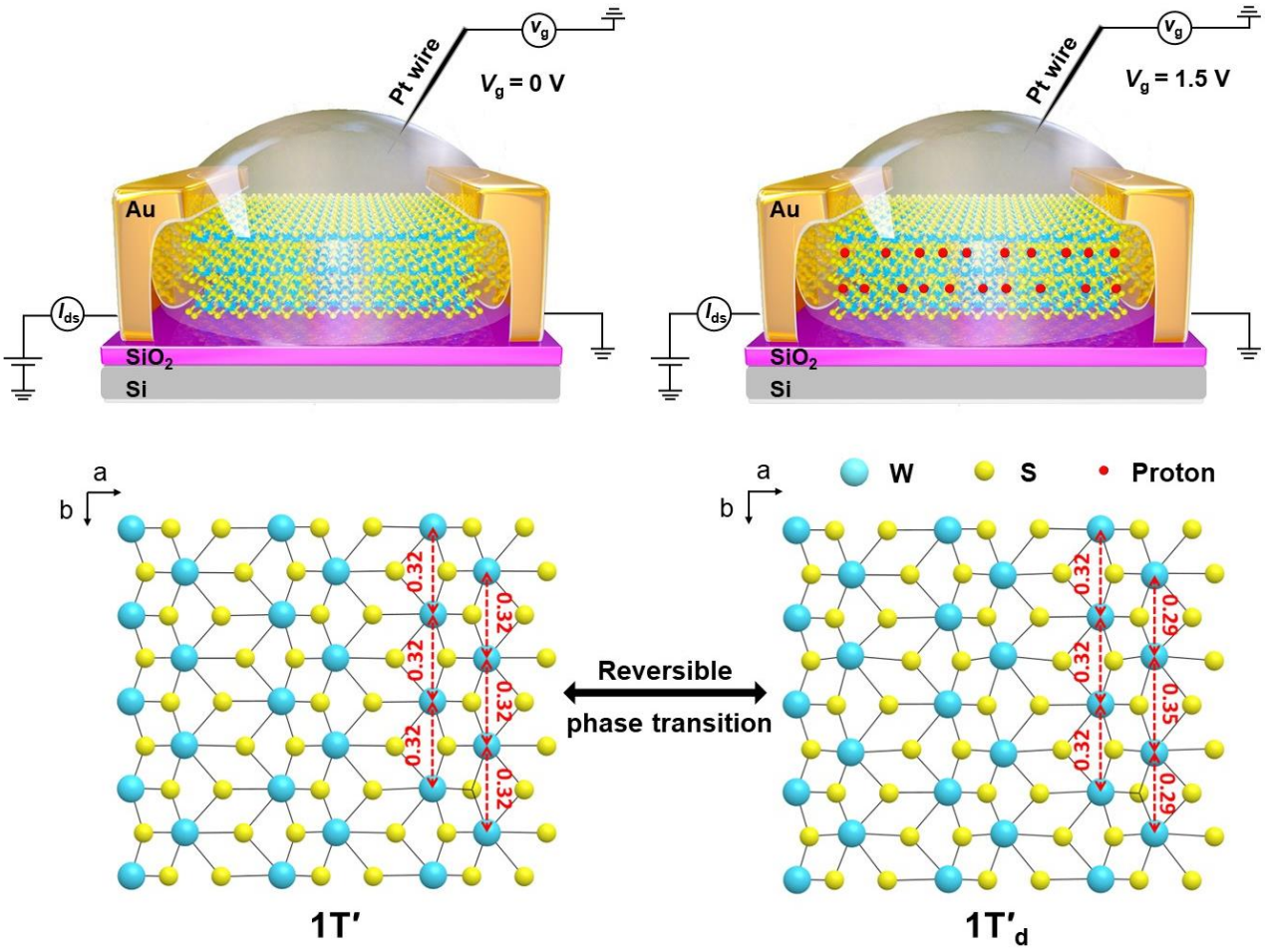
Pt wire
V_g
V_g = 0 V
Au
I_{ds}
SiO_2
Si
Pt wire
V_g
V_g = 1.5 V
Au
I_{ds}
SiO_2
Si
a
b
0.32
0.32
0.32
0.32
0.32
0.32
Reversible
phase transition
W
S
Proton
a
b
0.32
0.29
0.32
0.35
0.32
0.29
1T′
$1T'_d$